Geomechanics and Engineering, *Vol. 22, No. 5 (2020) 385-396*
DOI: https://doi.org/10.12989/gae.2020.22.5.385

Mechanical properties and failure mechanisms of sandstone with pyrite concretions under uniaxial compression

Shao J. Chen[1a], Meng Z. Ren[1b], Feng Wang*[1,2], Da W. Yin[1c] and Deng H. Chen[2d]

[1]College of Mining and Safety Engineering, Shandong University of Science and Technology, Qingdao, Shandong 266590, China
[2]Key Laboratory of Safety and High-efficiency Coal Mining, Ministry of Education, Anhui University of Science and Technology, Huainan, Anhui 232001, China

(Received December 21, 2019, Revised July 22, 2020, Accepted July 25, 2020)

Abstract. A uniaxial compression test was performed to analyse the mechanical properties and macroscale and mesoscale failure mechanisms of sandstone with pyrite concretions. The effect of the pyrite concretions on the evolution of macroscale cracks in the sandstone was further investigated through numerical simulations with Particle Flow Code in 2D (PFC2D). The results revealed that pyrite concretions substantially influence the mechanical properties and macroscale and mesoscale failure characteristics of sandstone. During the initial loading stage, significant stress concentrations occurred around the edges of the pyrite concretion accompanied by the preferential generation of cracks. Meanwhile, the events and cumulative energy counts of the acoustic emission (AE) signal increased rapidly because of friction sliding between the concretion and sandstone matrix. As the axial stress increased, the degree of the stress concentration remained relatively unchanged around the edges of the concretions. The cracks continued growing rapidly around the edges of the concretions and gradually expanded toward the centre of the sample. During this stage, the AE events and cumulative energy counts increased quite slowly. As the axial stress approached the peak strength of the sandstone, the cracks that developed around the edges of the concretion started to merge with cracks that propagated at the top-left and bottom-right corners of the sample. This crack evolution ultimately resulted in the shear failure of the sandstone sample around the edges of the pyrite concretions.

Keywords: pyrite concretion; mechanical properties; failure mechanics; acoustic emission; discrete element method

1. Introduction

In nature, rocks form with different types of discontinuities such as cracks (Wong and Einstein 2009, Amann *et al*. 2014, Zhao *et al*. 2016, Sharafisafa *et al*. 2019, Li *et al*. 2019), joints (Chen *et al*. 2018, Zhao *et al*. 2015, Yin *et al*. 2017), and concretions (Greno *et al*. 1999, Ortiz *et al*. 2000, Gao *et al*. 2016, Lee *et al*. 2018, Bewick *et al*. 2018, Salimidelshad *et al*. 2019). Under an external loading, the mechanical properties and crack growth behaviour of rocks are affected by these discontinuities, which have different sizes, non-uniform distributions, and different strengths. These factors further influence the stability of the rock mass. Concretions are heterogeneous inclusions interbedded in sedimentary rock and possess a different composition from that of the surrounding rocks (Li *et al*. 2014). When the loading condition changes on the rock mass, these concretions affect the mode and severity of the rock failure. Cracks often form along the edges of the concretions to reduce the stress threshold for different types of failure (Liu *et al*. 2016), which results in multiple types of geotechnical and mining engineering disasters such as collapse (Wang *et al*. 2019a, b) and rib spalling (Wu *et al*. 2011, Chen *et al*. 2019). Similarly, in many artificial engineering structures, cement, concrete, and other engineering materials are often used to fill rock joints and planes to improve the strength and stability of rock masses (Janeiro 2009), particularly affecting the mechanical properties and crack growth behaviour of rock. These artificial fillings are remarkably similar to the concretions in natural rocks. Therefore, the effects of concretions on the mechanical properties and macroscale and mesoscale failure mechanisms of rock masses need to be considered.

The concretions change the homogeneity of rock, resulting in strain differences and local stress concentration inside the rock, which have a significant impact on the rock mechanical characteristics and the failure process. The initial crack occurring at the tip of the concretion is caused by stress concentration when the shape of the concretion is irregular (Greno *et al*. 1999, Ortiz *et al*. 2000). This indirectly affects the subsequent crack development and the final failure mode. The probability of crack initiation at the tip is also different at different load levels. In general, the particle size of concretions is different from the rock matrix, such as calcite in coal (Gao *et al*. 2016). The particle size of

*Corresponding author, Ph.D.
E-mail: wangfeng@sdust.edu.cn
[a]Professor
E-mail: csjwyb@163.com
[b]M.Sc.
E-mail: 865001406@qq.com
[c]Ph.D.
E-mail: 949251142@qq.com
[d]Professor
E-mail: ahhncdh@163.com

ISSN: 2005-307X (Print), 2092-6219 (Online)

calcite significantly affects the peak strength and elastic modulus of coal and reduces its brittleness. When the stiffness of the concretion structure increases (Lee *et al.* 2018, Bewick *et al.* 2018, Salimidelshad *et al.* 2019), the number of cracks also increase. In addition, several studies (Zaitsev *et al.* 1981, Maji *et al.* 1991, Janeiro and Einstein 2010, Zhu *et al.* 2019, Leite *et al.* 2019) have explored the effect of concretions on rock mechanics and failure characteristics under a single factor (number, shape, or size) by preparing rock-like samples containing concretions. The results show that the presence of relatively stiff inclusions can provide better support and improvement to the post-failure concretion integrity of the rock. The stronger the mechanical properties of the concretions, the more the number of cracks that occur, which affect the final failure mode of the samples.

Therefore, in the present study, most of these studies focused on artificial concretions, which are typically weaker than the rock matrix. Few studies have explored the impact of natural concretions on the rock strength of engineered rock masses. The failure evolution of rock samples with concretions at the macroscale and mesoscale has also received limited attention. In this study, a uniaxial compression test was performed to analyse the mechanical properties and macroscale failure characteristics of sandstone containing pyrite concretions. The evolution of microscale cracks was further explored based on the acoustic emission (AE) behaviour and scanning electronic microscope (SEM) images of the samples. Numerical simulations were performed with Particle Flow Code in 2D (PFC2D) to analyse the crack propagation and aggregation patterns inside the samples.

2. Rock samples and testing procedure

2.1 Formation and component analysis of pyrite concretion

The sandstone samples used in the test were taken from the roof strata of a mine in Xuzhou, Jiangsu, China. First, sandstone samples with a diameter of 50 mm were extracted from rock blocks with a core-drilling machine. Subsequently, these samples were cut into cylinders with the desired height through the use of a stone-sawing machine. Finally, both ends of the cylindrical samples were polished with a grinding machine. During the sample preparation process, the parallel misalignment and diameter deviation between the two end faces needed to be less than 0.01 mm and 0.02 mm, respectively. The final test samples were standard cylinders with dimensions of Φ50 mm × 100 mm, as shown in Fig. 1(a). Among these, Y-1, Y-2, and Y-3 were sandstone samples with concretions, while N-1, N-2, and N-3 were conventional sandstone samples. In addition, certain concretion samples were extracted from the sandstone, ground into powder, and tested by X-ray diffraction (XRD). The test results are shown in Fig. 1(b). The characterisation results for the minerals in the concretion were consistent with the spectra of pyrite, quartz, and bauxite in international standard powder diffraction files (PDFs). In particular, the results indicated that the concretions comprised 66.8% pyrite, 22.5% quartz, 8.2% bauxite, and 2.5% of other materials.

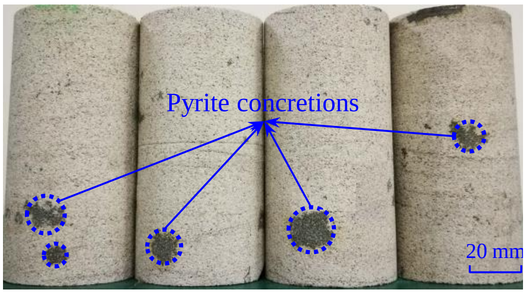

(a) Sandstone samples

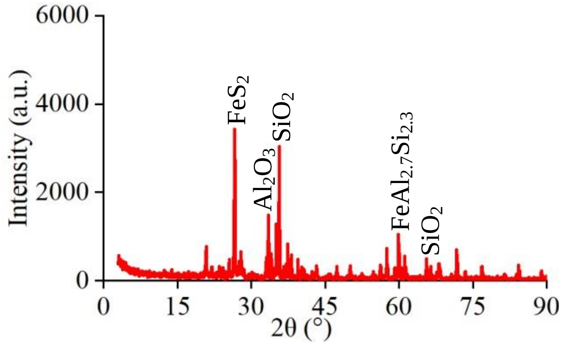

(b) X-ray diffraction of pyrite concretions

Fig. 1 Samples and component analysis

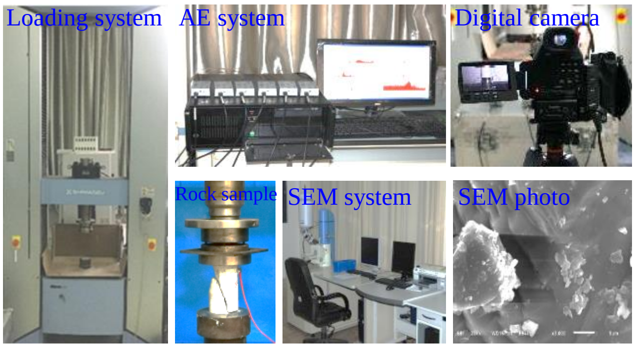

Fig. 2 Control and monitoring system

2.2 Experimental setup and monitoring techniques

The main control and monitor systems used in the experiment are shown in Fig. 2 and include the loading system, AE system, SEM, and digital video recording system. During the experiment, the loading system, AE system, and digital video recording system were operated simultaneously to ensure that they shared the same time parameter. This setup made it more convenient to process the data and analyse the results.

A Shimadzu AG-X250 precision universal testing machine was used as the loading system. The universal testing machine is powered by an AC motor servo drive. A double-screw drive mechanism is used to apply a load. The universal testing machine possesses good reliability and high precision, and it can be used to perform regular compression and tensile tests. The maximum load that could be applied during the experiment was 250 kN. A

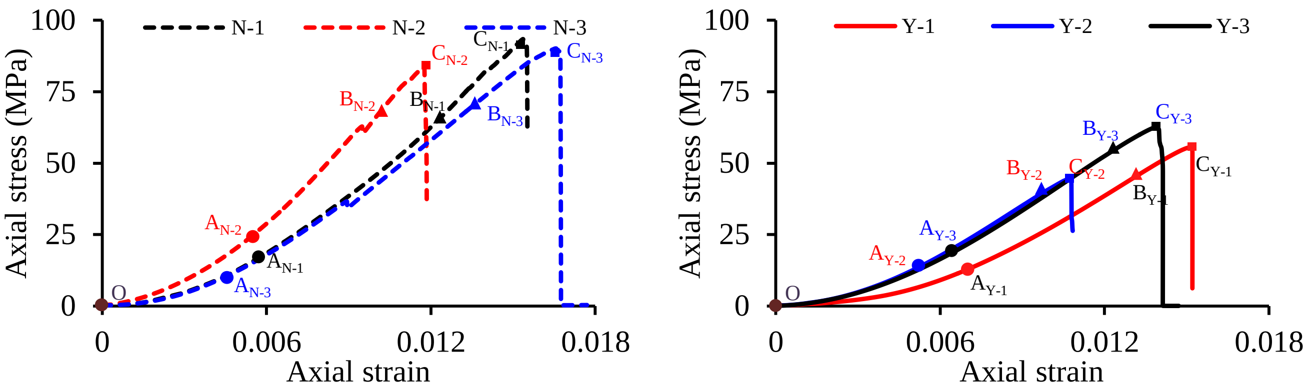

(a) Conventional samples (b) Samples with pyrite concretions

Fig. 3 Axial stress-strain curve of samples

Table 1 Results of uniaxial compression test

Number	Elastic modulus /GPa		Compressive strength /MPa		Stain in compaction stage /10^{-3}		Strain in unstable crack growth stage /10^{-3}		Peak strain /10^{-3}	
	Result	Average	Result	Average	Result	Average	Result	Average	Result	Average
N-1	7.4		93.4		5.9		1.6		15.4	
N-2	9.5	7.6	83.9	89.2	5.8	5.6	1.2	2.0	11.8	14.6
N-3	6.0		90.2		5.1		3.1		16.6	
Y-1	5.2		55.5		7.0		1.4		15.1	
Y-2	5.5	5.6	44.2	54.1	5.4	6.3	0.7	1.1	10.6	13.2
Y-3	6.0		62.6		6.5		1.2		13.9	

displacement-based loading control method was used to perform the uniaxial compression test until the sample fractured. The loading speed was set to 0.01 mm/s.

The MISTRAS series PCI-2 AE system was used to monitor AE events. During the experiment, the main amplifier, threshold, floating threshold, probe frequency, and sampling frequency for the AE system were set to 40 dB, 45 dB, 6 dB, 100–600 kHz, and 10^6 s^{-1}, respectively. To ensure close contact between the sensor and test sample, Vaseline was applied between them as a coupling agent. This reduced the acoustic impedance mismatch and reflection loss of energy at the contact interface so that the AE signal could be better received by the sensor. The sensors were fixed to a sample with tape. A lead-break coupling test was performed prior to the experiment to ensure that all sensors had a signal magnitude of greater than 90 dB.

The JSM-6510LV High & Low Vacuum SEM was used to characterise the samples. The resolutions in high- and low-vacuum modes can reach 3 and 15 nm, respectively. The magnification can reach 50,000–300,000×. The acceleration voltage can be adjusted between 0.5 and 30 kV. During the test, the fractured samples were processed into 10 mm × 10 mm characterisation samples. During the preparation process, the surface to be examined by SEM was left intact. Subsequently, the characterisation samples were cleaned in an ultrasonication bath with ethanol to remove dust and oil adhering to the surface. Finally, the samples were coated with a 5-10 nm thick metal layer before being examined with the SEM.

3. Mechanical properties and failure characteristics of sandstone with pyrite concretions

3.1 Mechanical characteristics of sandstone with pyrite concretions

During the experiment, the testing data were collected simultaneously by the computer at a sampling interval of 0.5 s. The stress-strain curves of the test samples under uniaxial compression is shown in Fig. 3, and the basic physical and mechanical parameters are presented in Table 1. The average uniaxial compressive strength and elastic modulus of the conventional sandstone samples were 89.2 MPa and 7.6 GPa, respectively. The average uniaxial compressive strength and elastic modulus of the sandstone samples with pyrite concretions were 54.1 MPa and 5.6 GPa, respectively, which indicated decreases of 39.3% and 26.3%, respectively. This agreed well with past numerical simulation studies (Gao *et al*. 2016, Zhu *et al*. 2019), which validated the accuracy of the experiments performed in this study.

The average strains of the conventional sandstone samples during the compression phase (OA) and unstable crack growth phase (BC) were 5.6 × 10^{-3} and 2.0 × 10^{-3}, respectively; the average peak strain was 14.6 × 10^{-3}. The average strains of the sandstone samples with pyrite concretions during the compression phase (OA) and unstable crack growth phase (BC) were 6.3 × 10^{-3} and 1.1 × 10^{-3}, respectively; the average peak strain was 13.2 × 10^{-3}. During the compression phase, the strain of sandstone with pyrite concretions was mainly caused by the compression of voids in the sandstone matrix, in the pyrite concretions, and at the interface between the pyrite concretions and sandstone matrix. However, the strain of the conventional sandstone sample was primarily caused by the compression of voids in the sandstone matrix alone. Therefore, the sandstone with pyrite concretions showed a 12.5% higher strain than the conventional sandstone during the compression phase. Cracks were first generated around the edges of the pyrite concretions, which also promoted crack propagation. These two factors reduced the strain of the sandstone with pyrite concretions during the unstable crack growth phase and peak strain by 45% and 9.6%, respectively, compared to the conventional sandstone.

3.2 Failure characteristics of sandstone with pyrite concretions

Fig. 4 shows the final morphologies of the sandstone after failure. Three types of failure modes were observed for the conventional sandstone samples: tensile failure, shear failure, and combined tensile-shear failure. No cracks were observed on the surface of the test samples before the main crack formed. The fracture plane of the samples remained relatively flat at the macroscale. However, all sandstone samples with pyrite concretions failed by shear along the edges of the concretions. Furthermore, the fracture plane was quite rough at the macroscale, particularly near the pyrite concretions. The presence of pyrite concretions determined the failure mode of the samples. This result is closely related to the genesis of pyrite concretion. Sub-circular pyrite concretions mostly form by physical and chemical interactions during the early diagenesis stage and are much stronger than intact rocks. When subjected to stress, pyrite concretions do not fracture by cracking easily because of their high strength. Instead, because stress concentrations often occur near their edges, cracks are mostly generated around them. Therefore, cracks propagating far from the concretions merge with the cracks propagating near the concretion edge, which eventually results in shear failure along the edges of pyrite concretions.

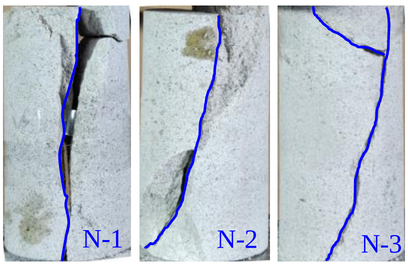

(a) Conventional samples

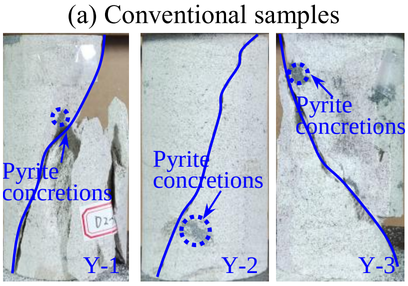

(b) Samples with pyrite concretions

Fig. 4 Failure modes of samples

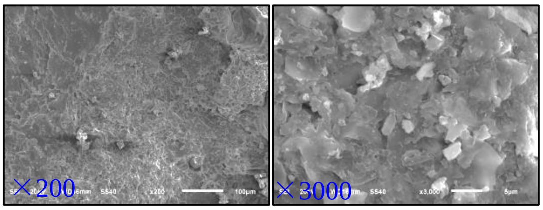

(a) Conventional samples

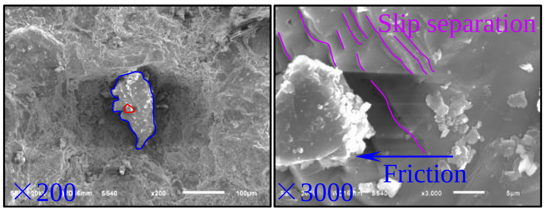

(b) Samples with pyrite concretions

Fig. 5 Scanning electron microscope results

To analyse the effect of pyrite concretions on the failure behaviour of sandstone at the microscale, the fracture planes of the N-2 and Y-2 sandstone samples after failure were examined with the SEM at 200× and 3000× magnification. The SEM images of the fractures are shown in Fig.5.

The cracks in the conventional sandstone sample had sufficient time to grow and expand into a macroscale fracture plane under axial stress. Therefore, the fracture plane was relatively flat and smooth, while the cracks were relatively underdeveloped at the fracture plane. Such behaviour resulted in the relative absence of other cracks on the surface of the conventional sandstone sample and a relatively flat fracture plane at the macroscale (Fig. 4(a)). However, different features were observed for the sandstone with pyrite concretions. Because the pyrite concretions are stronger than the sandstone matrix, they are more difficult to fracture under axial stress. Instead, the cracks continued to grow and propagate along the edges of the pyrite concretions. During the crack growth and propagation, the pyrite concretions were unlikely to fracture and thus experienced significant friction sliding along the surface of the sandstone matrix. In particular, saw-tooth trails and friction scratches were clearly observed on the microscale fracture plane. Large amounts of cement particles were observed on the friction sliding plane between the pyrite concretion matrix and sandstone matrix. At the macroscale, the fracture plane of the sample with pyrite concretions was more rugged, particularly near the concretions (Fig. 4(b)).

3.3 AE characteristics of sandstone with pyrite concretions

Fig. 6 shows the changes in the stress, AE events, and cumulative energy counts over time according to the experimental results. Based on the cumulative energy count curve, the evolution of the AE parameters can be divided into three periods: the quiet period, rising period, and active period. The division of "quiet period, rising period, and active period" is based on the moments when the AE count increases significantly. Owing to space limitations, samples N-1 and Y-1 are shown in Fig. 6 as representative

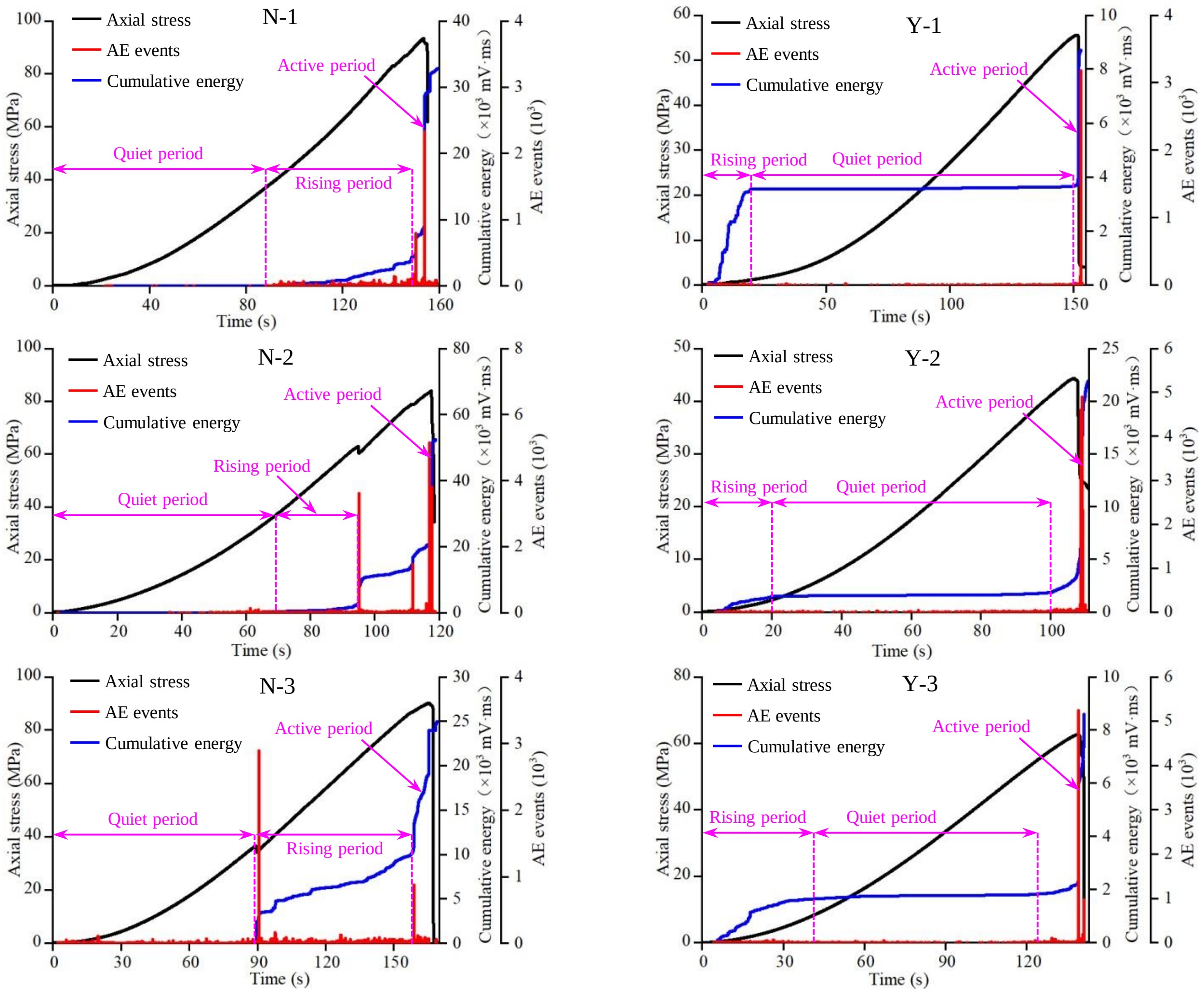

(a) Conventional samples (b) Samples with pyrite concretions

Fig. 6 Acoustic emission characteristics

examples for the analysis on the impact of pyrite concretions on the AE characteristics.

As shown in Fig. 6(a), the evolution of the AE parameters for the conventional sandstone sample comprised a quiet period, rising period, and active period. During the initial loading stage, the closing and sliding of the intrinsic gap released a small amount of elastic stress waves. The AE energy released during this stage was very low. Therefore, there were very few AE events and no significant increase in the cumulative energy associated with AE. When the axial stress exceeded 37.2 MPa, the AE parameters started to rise stably. During this stage, the cracks experienced intense growth and expansion with a very slow propagation speed. The number of AE events started to increase at a slow rate. While the cracks were already growing and expanding before the end of the rising period, this process had not yet reduced the strength of the sandstone. In other words, the axial strength of the sandstone had not yet been reduced. When the cumulative energy approached the critical value for accelerated crack expansion, the local cracks started to propagate rapidly. At this point, the AE events started to increase at a high rate, which indicated the active period. During this period, the AE events increased more than tenfold and were accompanied by a sharp increase in the cumulative energy counts. Before the peak strength was reached, the rapid crack propagation resulted in several small stress drops in the stress-strain curve that corresponded to the intermittent expansion of cracks; these were accompanied by a drastic increase in the cumulative energy counts of the AE signal.

As shown in Fig. 6(b), the AE parameters of the sandstone sample with pyrite concretions experienced a rising period, quiet period, and active period in succession. During the initial loading stage, a rising period was observed, where the AE changed and the cumulative energy count curve rose significantly. In addition, intense AE events were collected during this period. These features indicate that stress was concentrated near the pyrite concretions and that friction sliding occurred between the pyrite concretions and sandstone matrix, which released energy. During the quiet period, the cumulative energy count curve became relatively smooth. No sharp increase in the AE events was observed. In general, the quiet period had quite a few AE events. The AE events fluctuated slightly, and the cumulative energy count curve rose stably.

During the active period, cracks inside the sandstone

Table 2 Mesomechanical parameters

Parameters	Emod/GPa	Krat	Fric	Pb_emod/GPa	Pb_krat	Pb_ten/MPa	Pb_coh/MPa
Rock matrix	1.49	1.4	0.5	3.2	1.4	16.0	23.7
Pyrite accretion	1.69	1.0	0.5	4.0	1.0	24.0	30.0

sample grew much more intensely. Several cracks merged and penetrated throughout the sample. A significant amount of elastic energy accumulated inside the sample was rapidly released, which led to extremely frequent occurrences of AE events, a sharp increase in AE events, and a drastic rise of the cumulative energy count curve. The AE signal only intensified rapidly just before the moment of failure. This feature suggests that the cumulative energy increased rapidly in a short time. Apparently, the main crack propagated almost instantaneously. Such a characteristic is consistent with the instant destruction of the sample at the end of the test. This behaviour shortened the unstable crack growth phase inside the sample with pyrite concretions.

4. Macroscopic crack initiation characteristics of sandstone with concretions

4.1 Numerical model and microscale parameters

A PFC2D numerical simulation was performed to analyse the propagation pattern of the cracks in sandstone with pyrite concretions under uniaxial compression. Because the sandstone that was extracted onsite contained sub-circular pyrite concretions (Fig. 1(a)), the concretions were simplified as spheres in the numerical simulation. Based on the Y-3 sample, the mesoscale mechanical parameters were adjusted repeatedly by trial and error, and we used a control variable method until the mechanical characteristics of the numerical model were close to those of the physical model (Itasca Consulting Group 2008). The detailed procedure was as follows. First, a parallel bond model was selected for the simulation to better reflect the contact force between the particles in the rock. The effective modulus (emod) of the linear contact was kept at a relatively small value, the effective parallel bond modulus (pb_emod) was variable, and all other parameters were set to relatively large values. Then, the parallel bond modulus was derived by fitting the function between the tensile modulus and effective parallel bond modulus. The values were substituted for calibration. Subsequently, the linear contact modulus was obtained by fixing the parallel bond modulus and solving for the fitting function between the linear contact modulus and elastic modulus. Next, a proper stiffness ratio (kratio) was calculated by fixing the parallel bond modulus and linear contact modulus. The stiffness ratio of the parallel bond modulus and cohesion strength was calculated in a similar manner. Finally, the ideal mesoscale mechanical parameters were obtained through fine adjustment. The mesoscale mechanical parameters used in the numerical simulation are presented in Table 2. In total, 8898 particles were generated. The sizes of the rock matrix particles ranged from 0.35 mm to 0.45 mm, and the sizes of the concretion particles ranged from 0.25 mm to

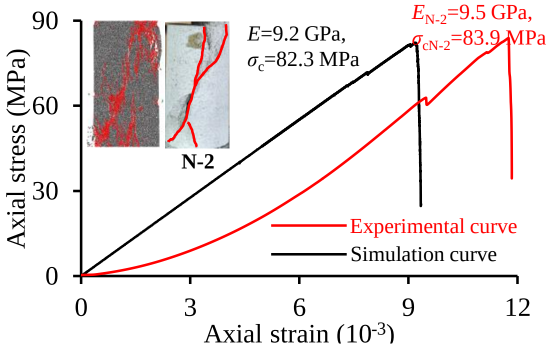

(a) Conventional samples

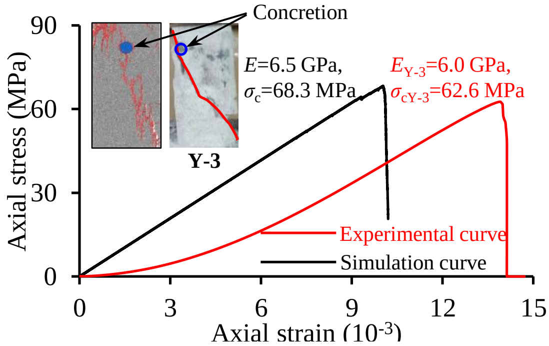

(b) Samples with concretions

Fig. 7 Comparison of experiment and numerical simulation

0.35 mm. The radius of the concretions was set to 5 mm. The bottom boundary was set as a fixed wall. Displacement-based loading was imposed on the top boundary with the same rate as that of the mechanical experiment.

Fig. 7 shows the stress-strain curve and failure modes obtained from the experiments and numerical simulation. The elastic modulus, peak strength, and failure modes from the numerical simulation were mostly consistent with those from the experiments. However, the stress-strain curve was not very evident during the initial compression phase in the numerical simulation. Prior to the peak stress, the stress-strain curve was almost linear, which indicates a linear deformation. In contrast to the experimental curve, the simulation curve was missing the crack compaction stage. The difference in the peak strain between the numerical and experimental curves is caused by the stress-strain curve from the simulation that cannot reflect the initial compression stage of the real rock. Therefore, the peak strain of the numerical simulation is lower than that of the laboratory test. To resolve this difference between the numerical simulation and experimental results, the mesoscale mechanical parameters in the simulation was adjusted as follows. After the deformation parameters and strength of the physical model were confirmed to be consistent with those of the numerical model, the elastic modulus, peak strength, and corresponding failure mode

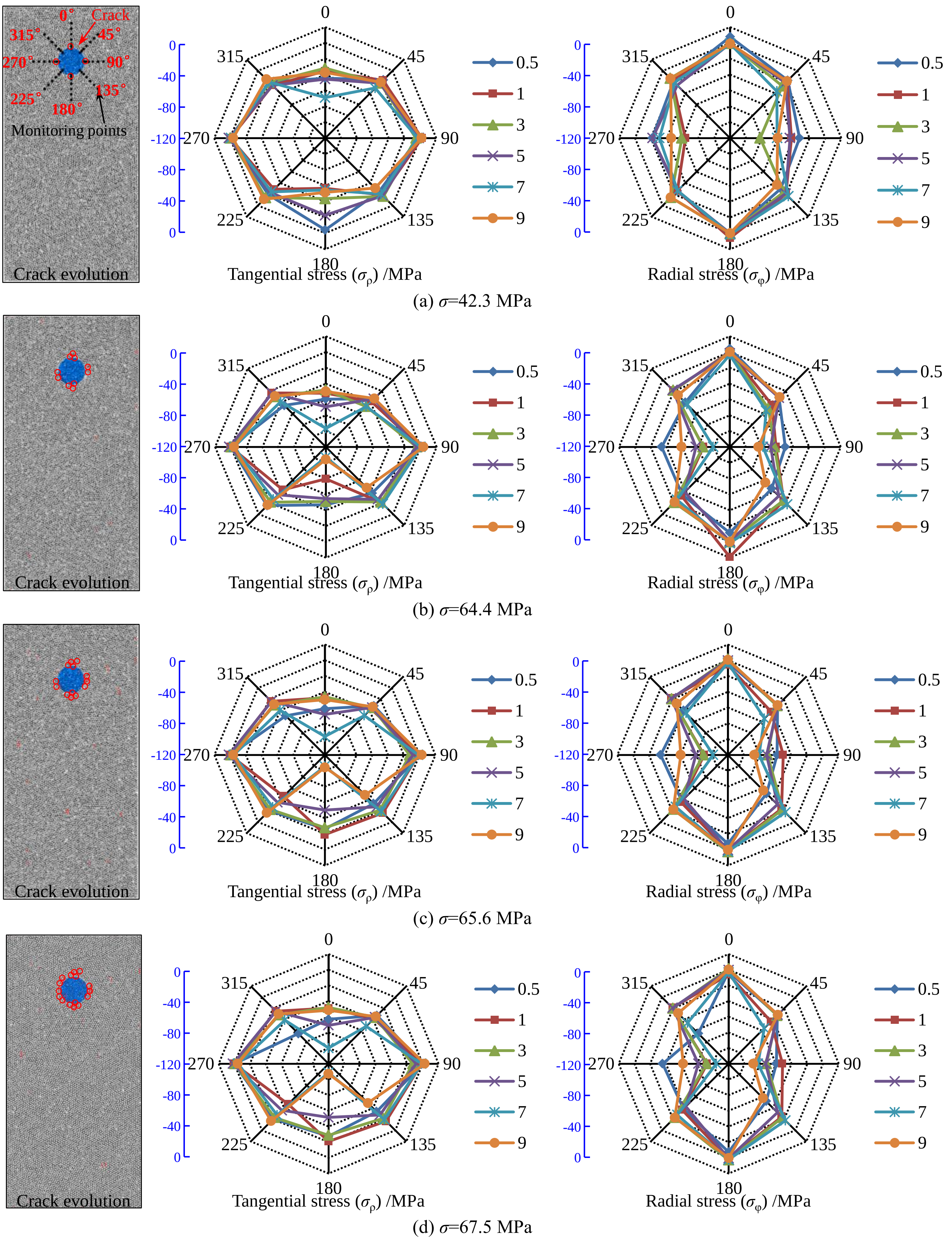

Fig. 8 Crack and stress evolution around concretion in numerical simulations

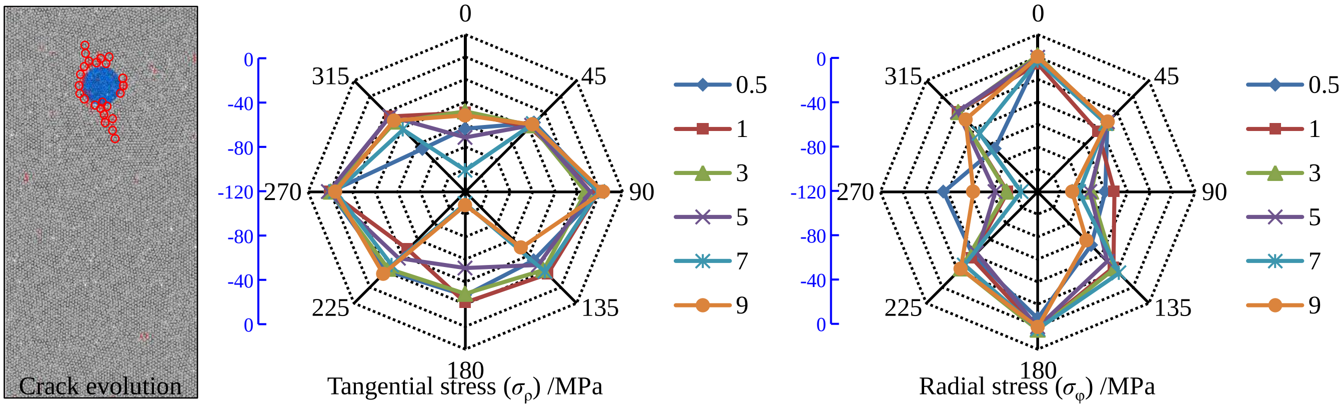

(e) σ=68.1 MPa

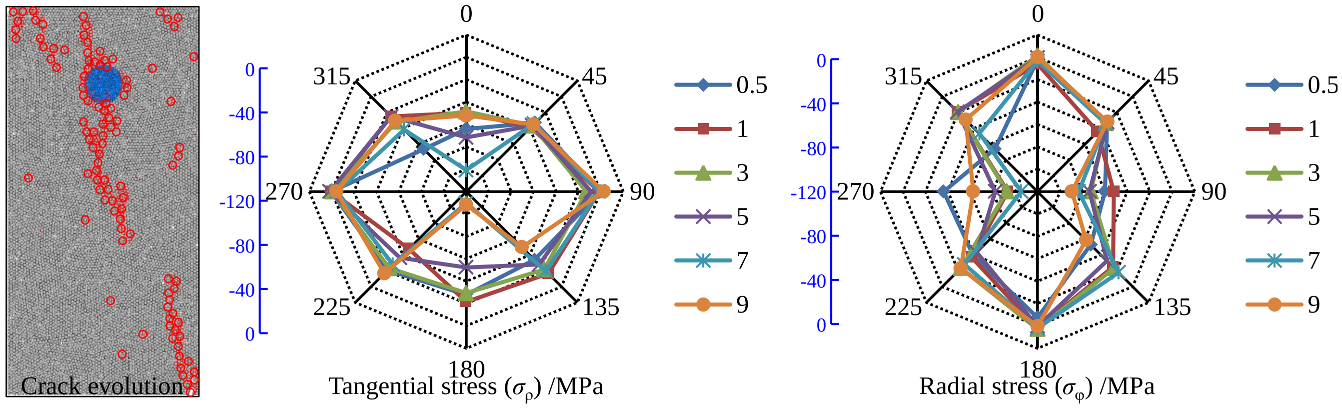

(f) σ=68.2 MPa

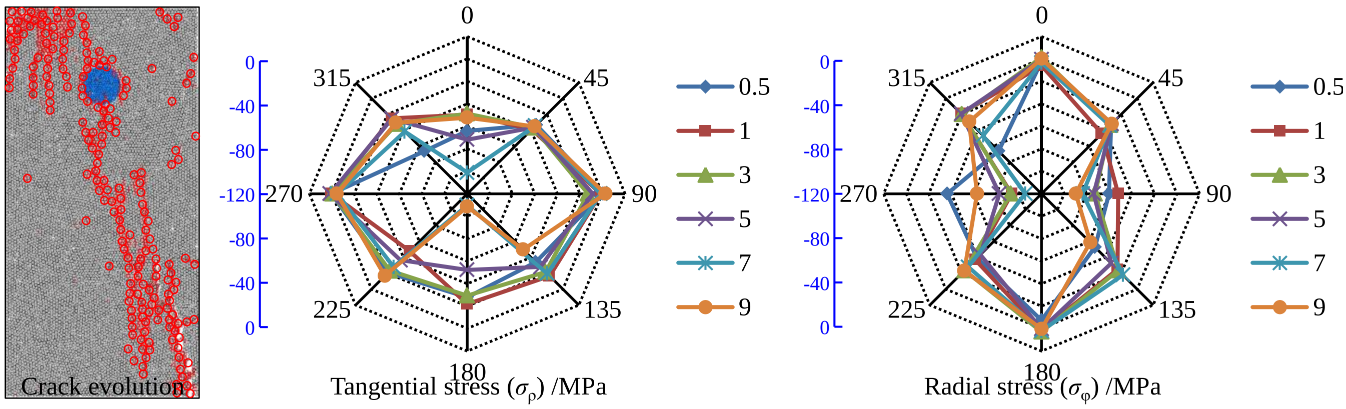

(g) σ=68.3 MPa

Fig. 8 Continued

obtained from the simulation needed to be as close to those obtained from the experiment as possible.

4.2 Crack initiation and stress evolution around concretions

Fig. 8 shows the evolution of the crack growth and expansion in the sample with pyrite concretions during the loading process. Eight representative characteristic time steps, which correspond to moments when the cracks start to appear or change significantly, were selected to give a better reflection of the failure process of the sample. Eight stress measurement lines were set up as shown in Fig. 8(a) to analyse the evolutions of the tangential stress (σ_φ) and radial stress (σ_ρ) near a concretion. These measurement lines were set at angles of 0°, 45°, 90°, 135°, 180°, 225° (-135°), 270° (-90°), and 315° (-45°), respectively. For each measurement line, six stress measurement circles were also arranged with a radius of 0.5 mm and centre-to-concretion-boundary distances of 0.5, 1.0, 3.0, 5.0, 7.0, and 9.0 mm. In total, 48 stress measurement circles were set. These circles were used to monitor the variations in the horizontal stress (σ_{xx}), vertical stress (σ_{yy}), and tangential stress (σ_{xy}) instantaneously during the numerical simulation. Based on these monitoring results, the tangential stress (σ_φ) and radial stress (σ_ρ) were calculated in the polar coordinate system based on the coordinate transformation formula for stress components in elastic mechanics (Xu 2008). Finally, the stress data at eight characteristic time steps were selected to plot the distribution radar chart of the tangential stress (σ_φ)

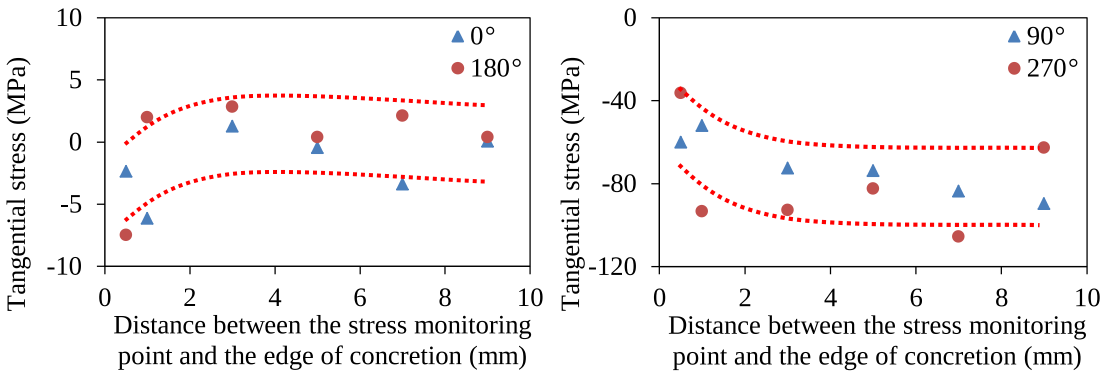

(a) Tangential stress (σ_φ)

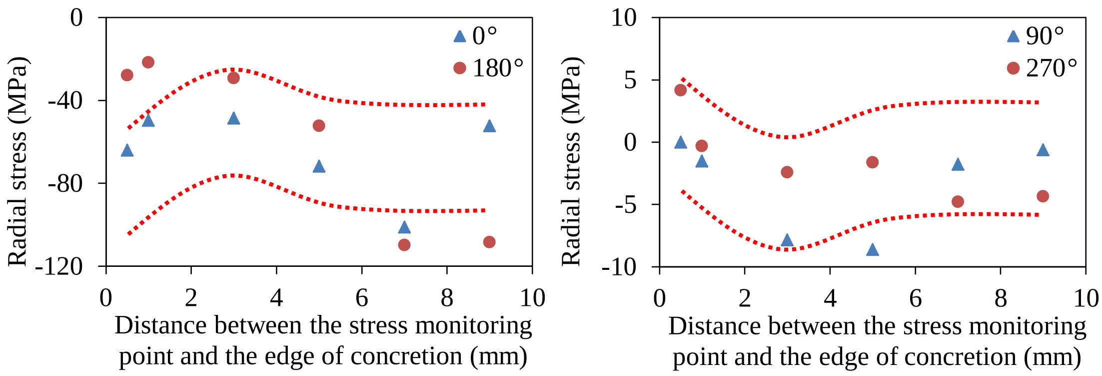

(b) Radial stress (σ_ρ)

Fig. 9 Stress distribution around concretion

and radial stress (σ_ρ), as shown in Fig. 8. During the axial stress loading process, the evolutions of the tangential stress (σ_φ) and radial stress (σ_ρ) and the growth and expansion of cracks near the concretion could be divided into four stages.

When the axial loading stress reached 42.3 MPa, the radial stress (σ_ρ) substantially increased along 0° and 180°, and the tangential stress substantially increased (σ_φ) along 90° and 270° (-90°). The concentration coefficients of the radial stress (σ_ρ) along the measurement lines at 0° and 180° were 1.63 and 1.34, respectively. The concentration coefficients of the tangential stress (σ_φ) along the measurement lines at 90° and 270° were 1.94 and 1.51, respectively. The stresses monitored at the other angles fluctuated around 0. The first set of cracks occurred near the edges of the concretion at 0°, 180°, 90°, and 270° (-90°), as shown in Fig. 8(a).

As the axial stress was gradually increased from 42.3 MPa to 65.6 MPa, the radial stresses (σ_ρ) along 0° and 180° and the tangential stresses (σ_φ) along 90° and 270° (-90°) continued to increase slowly. The cracks near the edges of the concretion at 0°, 180°, 90°, and 270° (-90°) started to grow and expand rapidly, as shown in Figs. 8(b) and 8(c). When the axial stress reached 67.5 MPa, the radial stresses (σ_ρ) along 45° and 225° (-135°) and the tangential stresses (σ_φ) along 135° and 315° (-45°) gradually started to rise. At the same time, the first set of cracks emerged near the concretion edges at 45° and 225° (-135°) and at 135° and 315° (-45°). These cracks started to merge with the cracks propagating at 0° and 180° and at 90° and 270° (-90°), as shown in Fig. 8(d).

When the axial stress reached 68.1 MPa, the radial stresses (σ_ρ) along 0° and 180° increased to 100.8 and 109.4 MPa, respectively, while the tangential stresses (σ_φ) along 90° and 270° (-90°) became 89.3 and 105.2 MPa, respectively. The cracks propagating at 0° and 180° started to grow and expand from the edges of the concretion towards the centre of the sample, as shown in Fig. 8(e)).

When the test sample fractured at the critical point in the numerical simulation, the cracks propagating at 0° and 180° continued to grow and expand from the edges of the concretion towards the centre of the sample. Meanwhile, crack groups propagating at the top-left and bottom-right corners of the sample propagated rapidly towards the concretion, as shown in Fig. 8(f). When the axial loading stress reached 68.3 MPa, the cracks propagating near the edges of the concretion merged with the crack groups propagating at the top-left and bottom-right corners of the sample. This created a main crack that penetrated the entire sample and caused it to fracture by shear failure along the edge of the concretion (Fig. 8(g)). The failure mode of the sample with a concretion in the numerical simulation was consistent with the experimental results.

As an example, Fig. 9 shows the distribution characteristics of the tangential stress (σ_φ) along 0° and 180° and radial stress (σ_ρ) along 90° and 270° (-90°) at an axial loading stress of 68.3 MPa in the numerical simulation. The distribution patterns of the tangential stress (σ_φ) and radial stress (σ_ρ) shown in Fig. 9 strongly agree with the stress distributions obtained by theoretical analyses in past studies (Janeiro and Einstein 2010, Goodier 1933, Tsuchina and Mura 1983, Lindeman *et al.* 1982). This consistency further validated the correctness of the numerical simulation in the present study. However, because the theoretical analyses assumed the research object to be continuous, homogenous, isotropic, and completely elastic, the stress values calculated from the numerical simulation were slightly different.

5. Influence mechanism of pyrite concretions on sandstone mechanics and failure characteristics

The research results indicated that pyrite concretions significantly impact the mechanical properties and microscale and mesoscale failure mechanisms of the sandstone. During the initial compression phase, a local stress concentration occurs near a concretion. Because the concretion is stronger, a strain difference is generated between the concretion and sandstone during the compression process. A large amount of energy is consumed by the sliding friction of the concretion in the sandstone matrix. Such behaviour leaves behind saw-tooth trails and friction scratches on the sandstone matrix. Meanwhile, the cumulative energy starts to rapidly increase, and the AE signal rises, which delays the quiet period of the AE. As the intrinsic gap between the sandstone matrix and concretion is compressed, a new void is generated at the same location, which increases the time for the internal gaps inside the sample to close up. Therefore, the strain of sandstone with pyrite concretions during the compression phase is mainly caused by the compression of voids in the sandstone matrix, in the pyrite concretion, and at the interface between the pyrite concretion and sandstone matrix. These factors are the major reasons for the prolonged compression phase of sandstone with concretions.

Once sandstone with concretions enters the linear elastic deformation phase, the level of the stress concentration near the concretion increases substantially. Cracks now first propagate at the edges of the concretion. Because the presence of concretions promotes crack expansion, fewer AE events are recorded during crack growth and expansion in this phase. The cumulative energy count curve keeps rising stably, and the AE enters the quiet period.

A further increase in the axial stress causes the sandstone with concretions to enter the unstable crack growth phase. The level of stress concentration near the concretion remains largely unchanged, while the cracks propagating near the concretion start to grow and expand rapidly. At the same time, the cracks propagating far from the concretion start to propagate towards it. Because the cracks cannot penetrate the concretion, which has high strength, these cracks merge with the old cracks propagating near the concretion during the initial stage. The regular merging and propagation of the cracks finally result in a short unstable crack growth phase. When the peak strength of the sandstone is reached, the energy accumulated earlier is dramatically released in a short amount of time. The crack starts to penetrate the entire sample rapidly with strong directionality. These behaviours reduce the peak strain and strength of the sandstone, and a main crack finally propagates within, causing it to fracture by shear failure along the edge of the concretion. During this process, the large amount of elastic energy that accumulated inside the sandstone during the unstable crack growth phase is dramatically released. The AE then enters the active period.

6. Conclusions

Based on the experiment and numerical simulations results, the following conclusions can be drawn:

- The strain of the sandstone with pyrite concretions increases during the compression phase compared to sandstone without concretions. In contrast, the sandstone with pyrite concretions exhibits a smaller strain during the unstable crack growth phase and a smaller peak strain.
- Owing to the friction sliding that occurs between the pyrite concretion and sandstone matrix. The cumulative energy count curve of AE rises rapidly and enters the rising period. As the pyrite concretion itself promotes crack growth, the cumulative energy count curve of AE rises slowly and enters the quiet period. When the sandstone with pyrite concretions is close to the critical failure condition, the cracks propagate and rapidly penetrate the sample with strong directionality. Thus, the AE signal intensifies instantly and enters the active period.
- The presence of pyrite concretions affects the failure mode of the sandstone. Three types of failure modes were observed for the conventional sandstone samples: tensile failure, shear failure, and combined tensile-shear failure. However, all sandstones with pyrite concretions fractured by shear failure along the edges of the concretions.
- The stress evolution and crack growth in the sandstone samples with concretions can be classified into four different stages. During the initial loading stage, there was a significant increase in the stress along the top-left and bottom-right corners of concretions and cracks first developed. As the load increased, the cracks started to form at 45° and 225° (-135°) as well as 135° and 315° (-45°) of the concretion and merge with the old cracks. As the axial load increased further, the cracks developing at 0° and 180° started to expand from the edges of the concretion towards the centre of the sample. Finally, the cracks near the concretion experienced rapid growth and merged with the surface crack groups propagating far away from the concretion. The merged crack penetrated the sample and caused the sample containing concretions to fracture by shear failure along the edge of the concretion.
- Because of the distinctive features of the concretions, the macroscale and mesoscale failure mechanisms of the rock are affected by a number of factors including the size, distribution density, and strength of the concretions. Future studies will focus on exploring the effects of concretions on the mechanical properties and macroscopic fracture mechanisms of rocks in greater depth.

Acknowledgments

This research is supported by the National Natural Science Foundation of China (51904162, 51904167), Shandong Provincial Natural Science Foundation, China (ZR2018BEE001), Taishan Scholars Project, SDUST

Research Fund (2019TDJH101) and Key Laboratory of Safety and High-efficiency Coal Mining, Ministry of Education (Anhui University of Science and Technology) (JYBSYS2019205). Additionally, we would like to thank Editage [www.editage.cn] for English language editing.

References

Amann, F., Undul, O. and Kaiser, P.K. (2014), "Crack initiation and crack propagation in heterogeneous sulfate-rich clay rocks", *Rock Mech. Rock Eng.*, **47**(5), 1849-1865. https://doi.org/10.1007/s00603-013-0495-3.

Bewick, R.P., Kaiser, P.K. and Amann, F. (2018), "Strength of massive to moderately jointed hard rock masses", *J. Rock Mech. Geotech. Eng.*, **11**(3), 562-575. https://doi.org/10.1016/j.jrmge.2018.10.003.

Chen, S.J., Qu, X., Yin, D.W., Liu X.Q. and Ma, H.F. (2018), "Investigation lateral deformation and failure characteristics of strip coal pillar in deep mining", *Geomech. Eng.*, **14**(5), 421-428. https://doi.org/10.12989/gae.2018.14.5.421.

Chen, S.J., Yin, D.W., Jiang, N., Wang, F. and Guo, W.J. (2019), "Simulation study on effects of loading rate on uniaxial compression failure of composite rock-coal layer", *Geomech. Eng.*, **17**(4), 333-342. https://doi.org/10.12989/gae.2019.17.4.333.

Gao, F.Q., Kang, H.P. and Wu, Y.Z. (2016), "Experimental and numerical study on the effect of calcite on the mechanical behaviour of coal", *Int. J. Coal Geol.*, **158**, 119-128. https://doi.org/10.1016/j.coal.2016.03.008.

Goodier, J.N. (1933), "Concentration of stress around spherical and cylindrical inclusions and flaws", *J. Appl. Mech.*, **1**, 39-44.

Greno, G.L., Otegui, J.L. and Boeri, R.E. (1999), "Mechanisms of fatigue crack growth in Austempered Ductile Iron", *Int. J. Fracture*, **21**(1), 35-43. https://doi.org.10.1016/s0142-1123(98)00055-3.

Itasca Consulting Group. (2008), PFC^{2D} (Particle Flow Code in 2 Dimensions) fish in PFC^{2D}, Itasca Consulting Group, Minneapolis, U.S.A.

Janeiro, R.P. (2009), "The effect of inclusions in brittle material", Ph.D. Dissertation, Massachusetts Institute of Technology, Cambridge, Massachusetts, U.S.A.

Janeiro, R.P. and Einstein, H.H. (2010), "Experimental study of the cracking behavior of specimens containing inclusions under uniaxial compression", *Int. J. Fracture*, **164**(1), 83-102. https://doi.org/10.1007/s10704-010-9457-x.

Lee, H.P., Olson, J.E. and Schultz, R.A. (2018), "Interaction analysis of propagating opening mode fractures with veins using the discrete element method", *Int. J. Rock Mech. Min. Sci.*, **103**, 275-288. https://doi.org/10.1016/j.ijrmms.2018.01.005.

Leite, M.H., Boivin, V. and Corthesy, R. (2019), "Stress calculation methods for overcoring techniques in heterogeneous rocks", *Int. J. Rock Mech. Min. Sci.*, **47**(7), 1180-1192. https://doi.org/10.1016/j.ijrmms.2010.06.002.

Li, D.Y., Han, Z.Y., Sun, X.L., Zhou, T. and Li, X.B. (2019), "Dynamic mechanical properties and fracturing behavior of marble specimens containing single and double flaws in SHPB tests", *Rock Mech. Rock Eng.*, **52**(6), 1623-1643. https://doi.org/10.1007/s00603-018-1652-5.

Li, J.X., Zhang, L.X. and Yang, L. (2014), *Mineral Petrology*, University of Electronic Science and Technology Press, Chengdu, Sichuan, China.

Lindeman, Z.R., Witemberg-Perzyk, D. and Perzyk, M.A. (1982), "A micromechanical prediction of elastic properties of composites with spherical particles", *J. Reinf. Plast. Comp.*, **1**(1), 3-15. https://doi.org/10.1177/073168448200100101.

Liu, G.F., Feng, X.T., Jiang, Q., Duan, S.Q., Yao, Z.B., Pei, S.F., Duan, X.P. and Zhou, M.X. (2016), "Failure characteristics, laws and mechanisms of rock spalling in excavation of large-scale underground powerhouse caverns in Baihetan", *Chin. J. Rock Mech. Eng.*, **35**, 865-878 (in Chinese). https://doi.org/10.13722/j.cnki.jrme.2015.0933.

Maji, A.K., Tasdemir, M.A. and Shah, S.P. (1991), "Mixed mode crack propagation in quasi-brittle materials", *Eng. Fract. Mech.*, **38**(2-3), 129-145. https://doi.org/10.1016/0013-7944(91)90077-e.

Ortiz, J., Cisilino, A.P. and Otegui, J.L. (2000), "Boundary element modelling of fatigue crack propagation in ductile iron", *Proceedings of the European Congress on Computational Methods in Applied Sciences and Engineering*, Barcelona, Spain, September.

Salimidelshad, Y., Moradzadeh, A., Kazemzadeh, E., Pourafshary, P. and Majdi, A. (2019), "Experimental investigation of changes in petrophysical properties and structural deformation of carbonate reservoirs", *Petrol. Explor. Dev.*, **46**(3), 565-575. https://doi.org/10.1016/S1876-3804(19)60036-4.

Sharafisafa, M., Shen, L.M., Zheng, Y.G. and Xiao J.Z. (2019), "The effect of flaw filling material on the compressive behaviour of 3D printed rock-like discs", *Int. J. Rock Mech. Min. Sci.*, **117**, 105-117. https://doi.org/10.1016/j.ijrmms.2019.03.031.

Tsuchina, E. and Mura, T. (1983), "On the stress concentration around a spherical inclusion", *J. Reinf. Plast. Comp.*, **2**(1), 29-33. https://doi.org/10.1177/073168448300200103.

Wang, F., Jiang, B.Y., Chen, S.J. and Ren, M.Z. (2019a), "Surface collapse control under thick unconsolidated layers by backfilling strip mining in coal mines", *Int. J. Rock Mech. Min. Sci.*, **113**, 268-277. https://doi.org/10.1016/j.ijrmms.2018.11.006.

Wang, F., Xu, J.L. and Xie, J.L. (2019b), "Effects of arch structure in unconsolidated layers on fracture and failure of overlying strata", *Int. J. Rock Mech. Min. Sci.*, **114**, 141-152. https://doi.org/10.1016/j.ijrmms.2018.12.016.

Wong, L.N.Y. and Einstein, H.H. (2009), "Systematic evaluation of cracking behavior in specimens containing single flaws under uniaxial compression", *Int. J. Rock Mech. Min. Sci.*, **46**, 239-249. https://doi.org/10.1016/j.ijrmms.2008.03.006.

Wu, W.P., Feng, X.T., Zhang, C.Q. and Qiu, S.L. (2011), "Classification of failure modes and controlling measures for surrounding rock of deep tunnel in hard rock", *Chin. J. Rock Mech. Eng.*, **30**(9), 1782-1802 (in Chinese). https://doi.org/10.1111/j.1759-6831.2010.00113.x.

Xu, Z.L. (2008), *Elasticity*, Higher Education Press, Beijing, China.

Yin, D.W., Chen, S.J., Chen, B., Liu, X.Q. and Ma, H.F., (2017), "Strength and failure characteristics of the rock-coal combined body with single joint in coal", *Geomech. Eng.*, **15**(5), 1113-1124. https://doi.org/10.12989/gae.2018.15.5.1113.

Zaitsev, Y.B. and Wittmann, F.H. (1981), "Simulation of crack propagation and failure of concrete", *Mater. Struct.*, **14**(5), 357-365. https://doi.org/10.1007/BF02478729.

Zhao, T.B., Guo, W.Y., Lu, C.P. and Zhao, G.M. (2016), "Failure characteristics of combined coal-rock with different interfacial angles", *Geomech. Eng.*, **11**(3), 345-359. https://doi.org/10.12989/gae.2016.11.3.345.

Zhao, W.H., Huang, R.Q. and Yan, M. (2015), "Mechanical and fracture behavior of rock mass with parallel concentrated joints with different dip angle and number based on PFC simulation", *Geomech. Eng.*, **8**(6), 757-767. https://doi.org/10.12989/gae.2015.8.6.757.

Zhu, Q.Q., Li, D.Y., Han, Z.Y., Li, X.B. and Zhou, Z.L. (2019), "Mechanical properties and fracture evolution of sandstone specimens containing different inclusions under uniaxial compression", *Int*. *J*. *Rock Mech*. *Min*. *Sci*., **115**, 33-47. https://doi.org/10.1016/j.ijrmms.2019.01.010.

CC